Ozaki et al. Earth, Planets and Space (2023) 75:111
https://doi.org/10.1186/s40623-023-01865-w

Earth, Planets and Space

FULL PAPER

Open Access

Linking the flow-induced tremor model to the seismological observation: application to the deep harmonic tremor at Hakone volcano, Japan

Tomonori Ozaki[1], Yohei Yukutake[1] and Mie Ichihara[1*]

Abstract

Decades ago, Julian (J Volcanol Geotherm Res 101:19–26, 1994. https://doi.org/10.1029/93JB03129) proposed the lumped parameter model of non-linear excitation of an elastic channel vibration by fluid flow as a mechanism of volcanic harmonic tremor. Since then, his model and similar flow-induced oscillation models have been applied or considered to explain volcanic tremors and low-frequency earthquakes. Here we extended Julian's model to allow quantitative comparison with observation data and applied it to deep harmonic tremor observed at Hakone volcano, Japan. We formulated the model in terms of the channel volume and linked the solution to the volumetric moment tensor. We also incorporated the turbulent flow effect to deal with both magma and super-critical fluid as the working fluid. Assuming the realistic material parameters at the tremor source depth ($\sim$ 30 km) beneath Hakone, we searched for the conditions in which tremor was generated at an observed frequency ($\sim$ 1 Hz). It is shown that both magma and super-critical fluids can generate realistic tremors with similar channel sizes of several-meter long and several-centimeter wide. We convolved the model solution with the Green's function at each seismic station to compare the model with the data. The result showed that Julian's model could produce synthetic tremor waveforms very close to the observed ones. Although the source waveform had only a single peak at each cycle, the convolved waveform exhibited an apparent secondary peak, like the observed waveforms. While the previous models generated such waveforms exhibiting alternative large and small peaks by a non-linear effect of period-doubling before the chaos, our model did not show such transitions, at least with the investigated parameters. Although most of the parameters and physical values of the solutions were in the realistic ranges, the only problem was the presumed low elasticity of the channel as small as 10^5 Pa to generate oscillation at $\sim$ 1 Hz. We proposed that not the rock property alone but the channel structure consisting of rock and compressible fluids could generate the low effective elasticity. To fully validate our model, the mechanism of such small elasticity should be identified, which is our future work.

Keywords Volcanic tremor, Flow induced oscillation, Non-linear oscillation

*Correspondence:
Mie Ichihara
ichihara@eri.u-tokyo.ac.jp
Full list of author information is available at the end of the article

Graphical Abstract

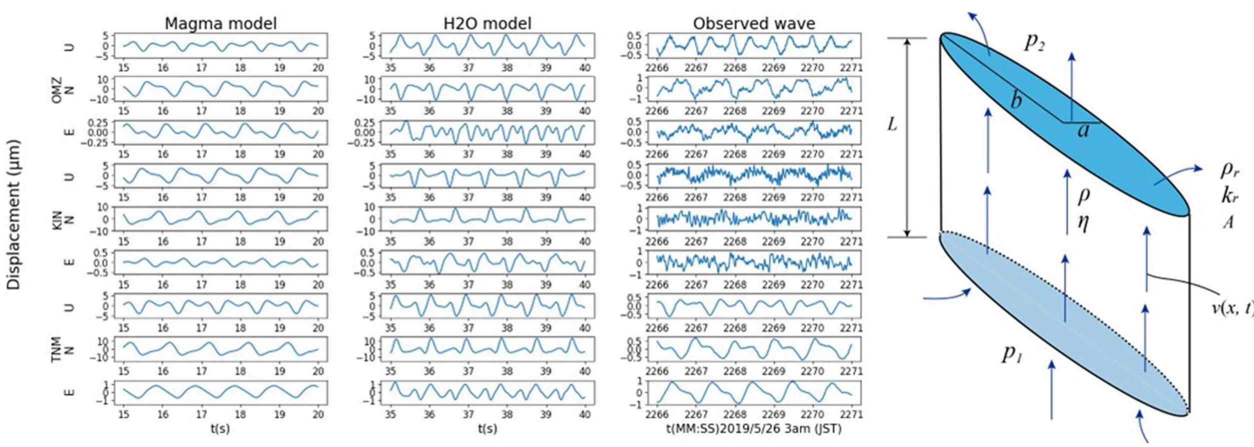

Introduction

A volcanic tremor is a continuous seismic signal that persists for several minutes or days and is sometimes accompanied by volcanic eruptions or independently. Among the various characteristics of volcanic tremors, a harmonic tremor, with spectral peaks corresponding to a fundamental frequency and additional overtones, is often observed (e.g., Hellweg 2000; Ichihara et al. 2013; Kamo et al. 1977; Konstantinou and Schlindwein 2002; Lees et al. 2004). While the source location of these harmonic tremors was usually estimated at shallow parts of volcanic edifices, mostly just beneath a conduit (e.g., Matsumoto et al. 2013; Maryanto et al. 2008; Ripepe et al. 2009) and not deeper than 10 km (e.g., Konstantinou and Schlindwein 2002; Matsumoto et al. 2013), a few studies report volcanic tremors radiated from the root of a volcano (Aki and Koyanagi 1981; Ukawa and Ohtake 1987).

Although a physical understanding of the volcanic harmonic tremors has been elusive, several generation mechanisms have been proposed. Julian (1994) proposed a lumped-parameter tremor model in which a non-linear oscillation was excited by fluid flow through an elastic plane-like channel within a volcanic edifice. Following the idea, various flow-induced oscillation models have been proposed theoretically and experimentally (e.g., Lyons et al. 2013; Rust et al. 2008; Corona-Romero et al. 2012; Takeo 2020). Another model considered elastic waves along the fluid-filled crack walls (Chouet 1988; Ferrazzini and Aki 1987; Dunham and Ogden 2012; Lipovsky and Dunham 2015). Hellweg (2000) discussed several possible fluid-dynamical periodic waves like a saw-tooth wave, generating the harmonic spectral feature. Specifically at a shallow depth, a magma-wagging oscillation around a magma column (Jellinek and Bercovici 2011), the growth and collapse of bubbles due to groundwater boiling (Leet 1988), the two-phase flow instability (Iwamura and Kaneshima 2005; Fujita 2008), the resonance of bubble clouds (Chouet 1996; Konstantinou et al. 2019), gas accumulation beneath permeable media (Girona et al. 2019), and the self-oscillations of fluid filling a cavity (Konstantinou 2015) were also proposed models for the harmonic or semi-monochromatic volcanic tremor.

Among the above tremor models, the flow-induced oscillation proposed by Julian (1994) (hereafter denoted as J94 model) is the most frequently considered in interpreting observed tremors. Because it is a lumped-parameter model, it is easy to calculate the oscillation of the source. On the other hand, the model parameters and calculated source time functions are not directly comparable with the observations. Therefore, the applications of the J94 model or other similar models have been limited to explain the oscillation mechanism (e.g., Lyons et al. 2013; Ichimura et al. 2018; Yamada et al. 2021) or non-linear features of waveforms and spectra (e.g., Hellweg 2000; Julian 2000; Konstantinou 2002; Hagerty and Benites 2003; Natsume et al. 2018). Recently, Natsume et al. (2018) and Takeo (2020) applied the J94 model or its extension to explain the waveforms of the harmonic tremor observed during the 2011 Shinmoe-dake eruption at the Kirishima volcano complex, Kyushu, Japan. Also, Natsume et al. (2018) showed that the J94 model could reproduce waveforms of the low-frequency earthquakes (LFEs) that occurred during the same eruption and had the same frequency components as the harmonic tremor. The data at Shinmoe-dake were assumed to represent the source waveforms because they were recorded within

1 km from the source. On the other hand, their models did not include the seismic wave radiation and did not evaluate the absolute amplitudes of the observed ground motions. Takeo (2020) noted that the tremor model only explains the qualitative characteristics of the observed phase portrait but emphasized that none of the other tremor models can explain the observed phase portrait.

To allow quantitative applications of the J94 model, we extended the model, linked between the model waveforms and seismic moment tensor, and clarified the relationship between the model parameters and geophysical parameters. This study tests the model with the harmonic tremor observed at a depth of $\sim$ 30 km beneath the Hakone volcano, central Japan (Yukutake et al. 2022). Although a few studies previously reported harmonic or monochromatic tremors that originated from the deep part beneath volcanoes, depth ranges from the lower crust to upper mantle (Aki and Koyanagi 1981; Ukawa and Ohtake 1987), deep LFEs that occurs within this depth range have been widely investigated (Aso et al. 2013; Hasegawa and Yamamoto 1994; Nichol et al. 2011; Yoshida et al. 2020; Oikawa et al. 2021). Yoshida et al. (2020) considered the J94 model as one of the possible mechanisms of the deep LFEs. On the other hand, Oikawa et al. (2021) precluded this possibility, assuming that the J94 model consisting of fluid movement would make a single force or dipole. This study associates the J94 model with the volumetric moment tensor. Our extension of the J94 model will be useful in the investigation of the deep tremors and LFEs, which are crucial to elucidate the feeding mechanism of magmatic fluid at depth (Matoza 2020).

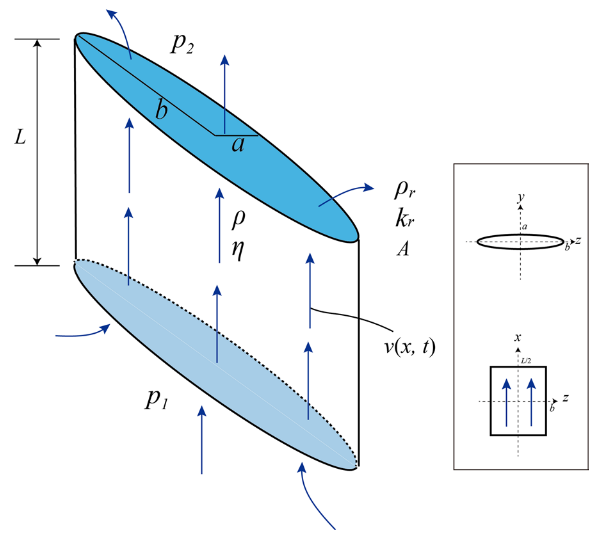

Fig. 1 The geometry of the tremor model, consisting of a thin channel connecting two large reservoirs (Julian 1994). The channel has an elliptical cross-section with half lengths of a and b ($\delta = a/b \ll 1$) and length L. The mean vertical flow speed is v, which is driven by the effective pressure difference between the upstream, p_1, and the downstream, p_2. The right-hand Cartesian coordinate (x, y, z) is taken with the x-axis in the flow direction and the y-axis parallel to the ellipse's minor axis. The inset figure shows the position of the channel projected onto the z–y and z–x planes. The origin of the coordinate axes is set at the center of the channel

Theory

We formulate a model for the oscillation induced by the viscous incompressible fluid flow in a thin channel connecting two reservoirs (Fig. 1). The fluid has the viscosity, η, and density, ρ. The system is embedded in the elastic host rock, having the Lamé constants, λ_r and μ_r, and density, ρ_r. The effective pressures (the pressure subtracted by the hydrostatic pressure of the fluid) in the upstream and downstream (p_1 and p_2, respectively) are constant, and their difference, p_1–p_2 (> 0), drives the flow. The fluid pressure in the channel changes with the flow speed, and the elastic channel deforms in response. The non-linear coupling between the flow and the channel generates the oscillation of the channel cross-section under certain conditions, which is derived by the linear stability analysis following J94. In the main text, we mainly explain our modification to the J94 model. The details of the derivation has been given in Supporting Information S1.

Equation of motion of the channel wall

Although J94 considered a two-dimensional flow between parallel plates, we approximate the channel cross section by an ellipse with half lengths of a and b ($\gamma \equiv a/b \ll 1$). Because of the thin geometry, the wall deformation is dominated by the change of the minor axis $a(t)$ with time, t, keeping $b \sim b_0$, where the subscript 0 is used to indicate the reference value. The cross-sectional area is $\alpha(t) = \pi b_0 a(t)$. The length along the flow is a constant, L. We define the right-hand Cartesian coordinate (x, y, z), with the x-axis in the flow direction and y-axis in the ellipse's minor axis direction. The coordinate origin is placed at the center of the channel (Fig. 1).

J94 formulated the equation of motion for the channel width h as

$$M'\ddot{h} + A'\dot{h} + k'(h - h_0) = F_p, \tag{1}$$

where the parameters of J94 are distinguished by the prime, and a dot and two dots indicate single and double differentiation with respect to time, respectively. The right-hand side, F_p, is the force on the two-dimensional channel wall exerted by the fluid pressure, which we discuss in "Resistive force for flow in the channel" section. On the left-hand side of Eq. (1), the first term represents the inertia. J94 approximated the effective mass, M', to be of order of $\rho_r L^2$. The second is the damping, and the coefficient A' was arbitrarily assumed. The third is the channel elasticity. To estimate k', J94 considered the opening of a dike, $\frac{w}{h} = \frac{\mu_r}{p(1-\nu)}$, where $\frac{w}{h}$ is the dike aspect ratio, and $\nu \equiv \frac{\lambda_r}{2(\lambda_r+\mu_r)}$ is the Poisson's ratio of the rock, and p is the overpressure. From this relation, J94 defined $k' = \mu_r \frac{L}{w}$ and assumed $\frac{L}{w}$ ranging from 0.01 to 0.1.

We modify Eq. (1) for the channel cross section as

$$C_m \rho_r \alpha_0 \frac{\ddot{\alpha}}{\alpha_0} + A\frac{\dot{\alpha}}{\alpha_0} + K_c k_r \frac{\alpha - \alpha_0}{\alpha_0} = \frac{F_p}{L}, \tag{2}$$

where the force due to the fluid overpressure on the right-hand side is

$$F_p = \int_{-L/2}^{L/2} p(x,t)\mathrm{d}x. \tag{3}$$

In Eq. (2), the effective mass and elasticity parameters explicitly include the rock density, ρ_r, and the bulk modulus, $k_r \equiv \lambda_r + \frac{2}{3}\mu_r$ with dimensionless coefficients, C_m and K_c.

We approximate

$$C_m^3 = \frac{L^2}{48\pi^2\alpha_0} = \frac{L^2}{48\pi^3 a_0 b_0}, \tag{4}$$

by the analogy of the effective mass that a spherical bubble in fluid feels on its expansion (Appendix 1). The representation of the elasticity in Eq. (2) refers to Mizuno et al. (2015). The coefficient K_c represents the reduction of the effective elasticity due to the shape and depend on the channel shape and the Poisson's ratio of the rock. Mizuno et al. (2016) provides a tool to calculate K_c, assuming $\lambda_r = \mu_r$ ($\nu = 1/4$), for an ellipsoidal cavity for given aspect ratios a_2/a_3 and a_1/a_3, where a_1, a_2, a_3 are the axial lengths of the ellipsoid ($a_1 < a_2 < a_3$). We may apply the tool to estimate K_c by substituting $(a_1, a_2) = (a, b)$ and assuming $a_3 \gg b$. We refer to values from this calculation but use K_c as a tuning parameter. It should be noted that $K_c k_r$ is not the effective bulk modulus of the host rock, but represents the elastic expansivity of the channel due to overpressure. For determining $K_c k_r$ for the thin channel, μ_r is more essential than k_r, as J94 formulated for k'.

Resistive force for flow in the channel

the pressure within the channel, p, is uniform in the y–z plane and depends on x and t. The flow speed averaged in the y–z plane is denoted as $v(x,t)$, which is subject to a resistive force, F_v, per unit cross section and unit length along the flow:

$$\begin{aligned} F_v(x,t) =& \frac{4\pi\eta}{\alpha}\left(\gamma + \frac{1}{\gamma}\right)v(x,t) \\ &+ \frac{C_d\rho|v(0,t)|}{4a}v(0,t), \quad \gamma \\ &+ \frac{1}{\gamma} \simeq \frac{\pi a_0^2}{\alpha}, \quad a \simeq \frac{\alpha}{\pi b_0}. \end{aligned} \tag{5}$$

The first term of the right-hand side works in the laminar flow regime with small Reynolds number, $R_e = 2a\rho v/\eta$. J94 used a corresponding term for a parallel-plane channel. We use the representation for an elliptic channel (Takeo, 2020). Considering $\gamma \ll 1$, we use the approximation of the second equation in (5). We introduce the second term to extend the model for turbulent flow conditions, where C_d is the friction factor of turbulent flow. We approximate $C_d = 0.01$ for simplicity (Wilson et al. 1980). For the tractability, the turbulent friction term is represented by the value at $x = 0$. The first term dominates the second when $R_e \ll 32/C_d = 3200$, which is consistent with the stability conditions of laminar flows between parallel planes ($R_e \leq 1000$) and in a circular pipe ($R_e \leq 1800$) (Landau and Lifshitz 1987).

Equations of motion

We consider the mass and momentum conservation in the channel and assume Bernoulli's theorem at the inlet and the exit of the channel, following J94. The detail is given in Supporting Information 1. Finally, we obtained the system equations, which are similar to those of J94.

The equation of motion of fluid is

$$\rho\dot{v} + \frac{4\pi^2 b_0^2\eta}{\alpha^2}v + \frac{\pi C_d \rho b_0}{4\alpha}|v|v = \frac{p_1 - p_2}{L}, \tag{6}$$

where $v = v(0,t)$, and all v hereafter denotes the value at $x = 0$. Replacing the corresponding equation of J94 by Eq. (6), the fluid pressure force F_p in Eqs. (2) and (3) is specified. Then, the equation of motion of the channel wall becomes

$$\left(C_m\rho_r + \frac{\rho L^2}{12\alpha}\right)\ddot{\alpha} + \left[\frac{A}{\alpha_0} + \frac{L^2}{12\alpha}\left(\frac{4\pi\eta}{\alpha}\frac{\pi b_0^2}{\alpha} - \frac{\rho}{2}\frac{\dot{\alpha}}{\alpha}\right)\right]\dot{\alpha} + K_c k_r \frac{\alpha - \alpha_0}{\alpha_0} = \frac{p_1 + p_2}{2} - \rho\frac{v^2}{2}. \tag{7}$$

Seismic moment tensor

The advantage of solving for the channel area is that we can relate the solution to the seismic moment tensor for the volume change, $\Delta V^C = L(\alpha - \alpha_0)$. The seismic moment tensor is directly related to the stress-free volume change, ΔV^T, instead of ΔV^C (Aki and Richards 2002; Ichihara et al. 2016). Because the expansion is dominated in the y-direction in the current model, we may approximate $\Delta V^T = \Delta V^C$, and the seismic moment tensor becomes (Mizuno et al. 2015)

$$\begin{pmatrix} M_{xx} & 0 & 0 \\ 0 & M_{yy} & 0 \\ 0 & 0 & M_{zz} \end{pmatrix} = 3k_r L\Delta\alpha \begin{pmatrix} 1/5 & 0 & 0 \\ 0 & 3/5 & 0 \\ 0 & 0 & 1/5 \end{pmatrix}, \quad (8)$$

where $\Delta\alpha \equiv \alpha - \alpha_0$.

Corona-Romero et al. (2012) developed a flow-induced oscillation model assuming a fluid-filled pipe buried in elastic half-space and calculated the far-field seismic waveforms using the so-called cylindrical source with the moment tensor component ratio of 1:2:2. Mizuno et al. (2015) presented that the volumetric moment tensor of a thin prolate ellipsoid differs from the cylindrical source model without ends along the axis. They also showed that the identical moment tensor representation (8) holds regardless of the existence of ends in the plane normal to the opening axis.

Tremor condition analysis

J94 presented the linear stability analysis to determine the conditions under which the flow excites the continuous oscillation. We made the same analysis for the modified model.

Steady flow solution

Equations (5) and (6) are transformed for the steady state with $v = v_s > 0$ and $\alpha = \alpha_s$ by setting all the time deviations to zero:

$$\frac{4\pi^2 b_0^2 \eta}{\alpha_s^2} v_s + \frac{\pi C_d \rho b_0}{4\alpha_s} v_s^2 = \frac{p_1 - p_2}{L}, \quad (9)$$

$$K_c k_r \frac{\alpha_s - \alpha_0}{\alpha_0} = \frac{p_1 + p_2}{2} - \rho \frac{v_s^2}{2}. \quad (10)$$

We solve Eqs. (9) and (10) numerically. Because both v_s, and α_s are positive, and all the parameters are also positive, a set of (v_s, α_s) is uniquely determined.

Linear stability analysis

Equations (6) and (7) are linearized considering small perturbation around the steady-state solution as $v = v_s + \hat{v}$ and $\alpha = \alpha_s + \hat{\alpha}$. The linearized equations are represented in the matrix form as

$$\frac{\mathrm{d}}{\mathrm{d}t}\begin{bmatrix} \hat{\alpha} \\ \dot{\hat{\alpha}} \\ \hat{v} \end{bmatrix} = \begin{bmatrix} 0 & 1 & 0 \\ -\frac{K_c k_r}{M_j + m_j} & -\frac{A + a_j}{M_j + m_j} & -\frac{\rho v_s \alpha_0}{M_j + m_j} \\ \frac{v_s}{\alpha_s}\left(\frac{2a_j}{m_j} + e\right) & 0 & -\left(\frac{a_j}{m_j} + 2e\right) \end{bmatrix} \begin{bmatrix} \hat{\alpha} \\ \dot{\hat{\alpha}} \\ \hat{v} \end{bmatrix}, \quad (11)$$

where (M_j, m_j, a_j) are defined to be comparable with (M, m, a) of J94 as

$$M_j \equiv C_m \rho_r \alpha_0, m_j \equiv \frac{\rho L^2 \alpha_0}{12\alpha_s}, a_j \equiv \frac{L^2\alpha_0}{12\alpha_s}\frac{4\pi^2 b_0^2 \eta}{\alpha_s^2} = m_j \Gamma, \quad (12)$$

where

$$\Gamma \equiv \frac{4\pi^2 b_0^2 \eta}{\alpha_s^2 \rho}. \quad (13)$$

In addition, the parameter e is defined to incorporate turbulent friction as

$$e \equiv \frac{\pi C_d b_0 v_s}{4\alpha_s}. \quad (14)$$

It is noted that e dominates Γ at large R_e and vice versa.

We express the characteristic equation of the matrix in (11) as

$$\lambda^3 + C_2\lambda^2 + C_1\lambda + C_0 = 0, \quad (15)$$

where

$$C_0 \equiv \frac{1}{M_j + m_j}\left[(\Gamma + 2e)K_c k_r + \frac{\rho v_s^2 \alpha_0}{\alpha_s}(2\Gamma + e)\right], \quad (16)$$

$$C_1 \equiv \frac{1}{M_j + m_j}\left[(\Gamma + 2e)(A + m_j\Gamma) + K_c k_r\right], \quad (17)$$

$$C_2 \equiv \frac{A + m_j\Gamma}{M_j + m_j} + \Gamma + 2e. \quad (18)$$

These coefficients are all positive. Therefore, as J94 derived, the condition for tremor to occur is

$$R \equiv \frac{C_0}{C_1 C_2} > 1, \quad (19)$$

and the angular frequency, ω, at the onset of instability is

$$\omega^2 = C_1. \tag{20}$$

Material Parameters

We assume that flow of magma or super-critical water drives the oscillation of channel. Since we model the oscillation at the lower crustal level, primary magma, namely basaltic magma, was assumed. The density (ρ) and viscosity (η) of basaltic magma at a depth of 30 km is assumed as 2800 kg/m^3 and 20 Pa s, respectively. The viscosity value is arbitrary because the temperature of the tremor source region has not been constrained. In the case of super-critical fluids, we assume an H_2O–CO_2 mixture with the CO_2 molar concentration of 0.6. The molar volume of the carbonated water under the conditions of 500 MPa and 500 °C are 34 cm^3/mol (Bowers 1995). The corresponding density is $\rho \sim 1010$ kg/m^3. The viscosity is approximated as 2×10^{-4} Pa s by extrapolating the data for super-critical pure H_2O from 2 to 100 MPa at 500 °C (JSME 1983) because it depends on the pressure only slightly up to 1 GPa (Audétat and Keppler 2004).

The elasticity is the problematic parameter when one wants to fit the observed tremor by the J94 model. We assumed that the channel wall is composed of the representative rocks at this depth. According to the tomographic result by Yukutake et al. (2021), the averaged P- and S-wave velocities at a depth of 21 km beneath the Hakone volcano are estimated at 6.7 km/s and 3.8 km/s, respectively. The P-wave velocity corresponds to the lower crust of Izu-arc composed of the gabbroic rock (Kodaira et al. 2007). According to Christensen (1996), we assumed the ρ_r of gabbro as 2968 kg/m^3 that forms the host rock around the channel. Given the tomographic result by Yukutake et al. (2021), elastic constant k_r of host rock is obtained as 76.1 GPa. The viscosity of channel wall can be negligible in the frequency range we considered.

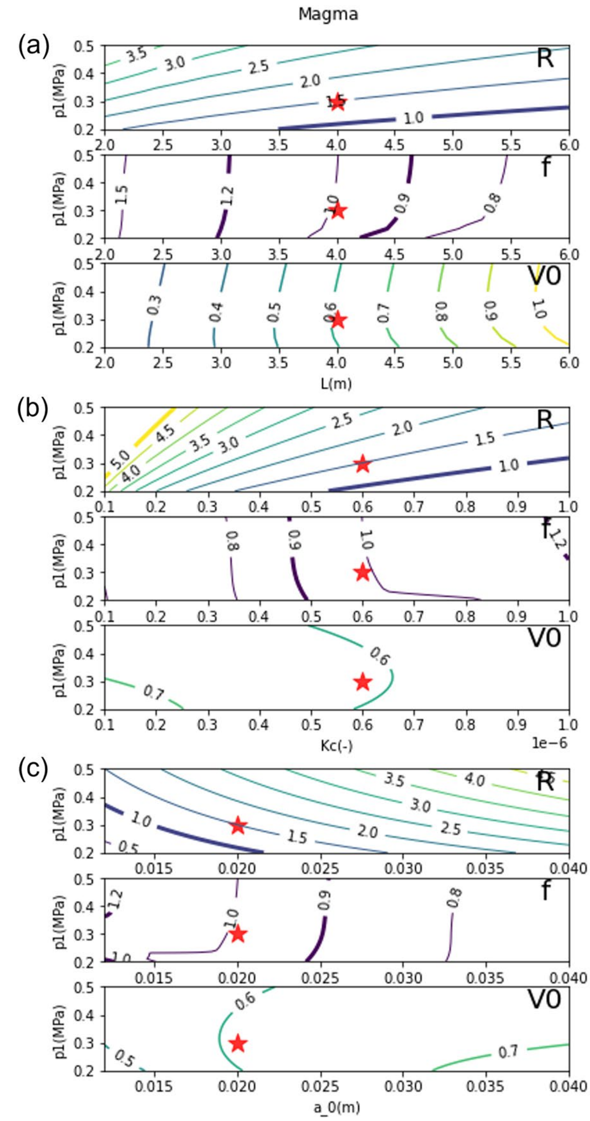

Fig. 2 Oscillation condition diagrams for magma ($\rho = 2800$ kg/m^3, $\eta = 5$ Pa s). The parameter R determining the tremor condition, the oscillation frequency, f, and the channel volume, $V_0 = L\alpha_0$, are shown from the top to the bottom as functions of the driving pressure, p_1, and either of the crack length, L (**a**), the channel elasticity coefficient, K_c (**b**), and the minor half width of the channel cross section, a_0 (**c**). In each frame, all the parameters except those on the axes are fixed at the values in Table 1

Numerical methods

Model calculations

To select adequate sets of parameters, we searched for conditions in which tremor occurs, represented by $R > 1$ in Eq. (19), and the oscillation frequency, f, is around 1 Hz, referring to the observation at Hakone. The main tuning parameters are the channel geometry (L, γ) and its elasticity coefficient K_c, and the driving pressure p_1. The dependence on b_0 was minor. We kept the downstream effective pressure at the lithostatic value, that is $p_2 = 0$.

For each set of parameters, we numerically solved Eqs. (9) and (10) to determine the steady-state solution (v_s, α_s). The variable α_s can be eliminated from the two equations to give a quartic equation in v_s, which is solved by a Python function, numpy.roots. We employed the solution satisfying $v_s > 0$ and $\alpha_s > 0$ and used them to calculate R and R_e, defined here by

Table 1 Parameters for magma flow

Parameter	Value	Unit	Definitions
a_0	0.02	m	Minor half axis of the channel cross section
b_0	1.0	m	Major half axis of the channel cross section
L	4.0	m	Length of the channel
C_m	0.813	–	$L^{\frac{2}{3}}(48\pi^3 a_0 b_0)^{-\frac{1}{3}}$: Eq. (4)
p_1	3.0×10^5	Pa	Upstream effective pressure
p_2	0.0	Pa	Downstream effective pressure
ρ	2800	kg/m^3	Fluid density
η	5.0	Pa s	Fluid viscosity
C_d	0.01	–	Turbulent friction factor
A	0.0	Pa s	Channel damping coefficient
K_c	6.0×10^{-7}	–	Channel elasticity coefficient
k_r	76.1×10^9	Pa	Bulk modulus of the host rock
ρ_r	2968	kg/m^3	Density of the host rock

Table 2 Parameters for hydrothermal flow

Parameter	Value	Unit	Definitions
a_0	0.02	m	Minor half axis of the channel cross section
b_0	1.0	m	Major half axis of the channel cross section
L	4.0	m	Length of the channel
C_m	0.813	–	$L^{\frac{2}{3}}(48\pi^3 a_0 b_0)^{-\frac{1}{3}}$: Eq. (4)
p_1	3.0×10^4	Pa	Upstream effective pressure
p_2	0.0	Pa	Downstream effective pressure
ρ	1010	kg/m^3	Fluid density
η	2.0×10^{-4}	Pa s	Fluid viscosity
C_d	0.01	–	Turbulent friction factor
A	0	Pa s	Channel damping coefficient
K_c	3.0×10^{-6}	–	Channel elasticity coefficient
k_r	76.1×10^9	Pa	Bulk modulus of the host rock
ρ_r	2968	kg/m^3	Density of the host rock

$$R_e \equiv \frac{2\alpha_s \rho v_s}{\pi b_0 \eta}, \tag{21}$$

where $\alpha_s/(\pi b_0)$ is the channel width in the steady state. On the other hand, f was determined from the numerical solutions of Eqs. (6) and (7). We obtained the solutions $(\alpha, \dot{\alpha}, v)$ as functions of the laps time, t, at 0.01-s intervals, with the initial condition of $(\alpha(0), \dot{\alpha}(0), v(0)) = (\alpha_0, 0, 0)$. The calculation was performed for 500 s, which was long enough to achieve the limit cycle at each condition. We picked the times at which α passed α_s with $\dot{\alpha} > 0$ by the linear interpolation for the last two cycles, sequentially as t_i $(i = 1, 2, 3)$. Then, we calculated the frequency by $f_i = 1/(t_{i+1} - t_i)$ $(i = 1, 2)$. When $|f_2 - f_1| < 0.01$ s^{-1}, we regarded that the solution reached the limit cycle and employed f_2 as f.

We used a Python function, scipy.integrate.solve_ivp to calculate the model equations, (6) and (7). The relative and absolute tolerances (r_{tol}, a_{tol}) were set at $(10^{-6}, 10^{-8})$ for magma and $(10^{-8}, 10^{-10})$ for super-critical fluids. We compared the solutions with those obtained using $(r_{tol}, a_{tol}) = (10^{-6}, 10^{-8})$ and $(10^{-8}, 10^{-10})$ for some cases and found no significant differences.

Comparison with the observation

To convert the source waveforms to the ground displacement at each station, we calculated the Green's function using OpenSWPC code based on the finite difference method developed by Maeda et al. (2017). We used the one-dimensional velocity structure beneath Tanzawa Mountains near Hakone (Hiraga 1987) that is an initial model for the tomographic study (Yukutake et al. 2021), including the topography information at the surface layer. We consider two models of seismic attenuation structure; (1) the homogeneous attenuation model in which Qp and Qs are set as 600 and 300, and (2) the one-dimensional attenuation model based on the result by Kashiwagi et al. (2020). We set the grid nodes at the interval of 0.03 km in the horizontal and vertical directions and 0.001 s in the direction of the time axis. We configured the rectangular computational region with a length of 24 km in the horizontal direction and from − 4 to 35 km in the depth direction, centered at the epicenter of the tremor source. Green's function was calculated for 20 s from the origin time. As a source model, we assumed an open crack, of which moment tensor is given in Eq. (8), oriented to the EW direction. The Green's function was calculated for the moment value of $M_0 \equiv M_{xx} + M_{yy} + M_{zz} = 10^9$ Nm. This value of M_0 is not essential because we normalize the Green's function by M_0 in taking the convolution with the source time function. We used the Kupper function with a duration time of 0.05 s as a source time function of the Green's function. Using this duration time, we can consider it a delta function with a flat spectral response below 10 Hz, which is applicable to our target observed tremor with a fundamental peak of 1 Hz. We also convolved the response of the velocity seismometer to compare the observed waveforms.

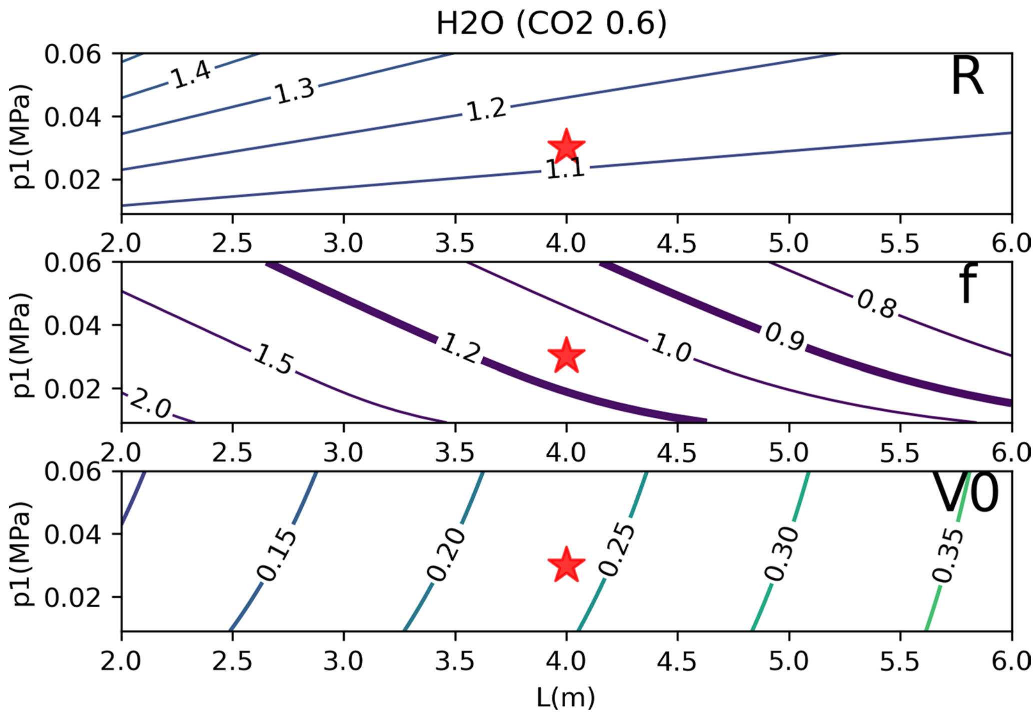

Fig. 3 Oscillation condition diagrams for super-critical fluid ($\rho = 1010$ kg/m^3, $\eta = 2 \times 10^{-4}$ Pa s). The format follows Fig. 2a

Results

Parameter search

We investigate the dependence of R, f, and the steady-state channel volume, $V_0 = \alpha_s L$, on the model parameters.

Figure 2 presents the result for magma as the work fluid. In Fig. 2a, we calculated Eqs. (9) and (10) to obtain v_s and α_s for the given parameters in Table 1 and various L and p_1 as on the axes. The bottom panel shows V_0 with contours of which values (m^3) are presented on the individual curves. Then, R is calculated by Eqs. (12)–(19) and presented in the top panel with contours. Because of condition (19), oscillation occurs in the parameter range above the contour of $R = 1$. In the region of $R > 1$, we solved Eqs. (6) and (7) and evaluated the frequency, f, as explained in the section, Model calculations. The frequency is shown in the middle panel by contours with values in Hz. Similarly, we investigated R, f, and V_0 as functions of K_c and p_1 (Fig. 2b) and the channel width $\alpha_0/(\pi b_0)$ and p_1 (Fig. 2c). The parameters except those on the axes are fixed as listed in Table 1. The Reynolds number, R_e, is smaller than 1000 in the displayed parameter ranges of Fig. 2, indicating laminar flow in the channel.

Also, Fig. 3 shows the corresponding results (only on the p_1–L space) for the hydrothermal fluid. The other parameters are fixed as listed in Table 2. In this case, the flow is turbulent ($R_e \sim 10^6$), for which the turbulent friction term in Eq. (5) works effectively.

Both Figs. 2 and 3 demonstrate that R increases as the driving pressure (p_1) increases, indicating that the oscillation is more effectively excited. It is interpreted as the result of the increasing flow speed. On the other hand, as L increases, it becomes more difficult for the oscillation to occur. The essential result here is that there are sets of parameters with which tremor was excited at a frequency around 1 Hz, as observed at Hakone volcano (Yukutake et al. 2022). We selected a representative set of parameters for each of magma and hydrothermal flows (Table 1), and calculated Eqs. (6) and (7) with the initial condition of $(\alpha, \dot{\alpha}, v) = (\alpha_0, 0, 0)$ (Fig. 4). In either case, continuous oscillation at $f \sim 1$ Hz is generated. The waveform has a non-linear wave characteristics with a sharp peak and a round trough. The non-sinusoidal periodic waveforms have harmonic spectra.The violent oscillation presented in Fig. 4b includes α and v_s almost zero in each cycle. The hydrothermal fluid more easily generates such violent oscillations than magma even with R close to unity. These waveforms are compared with the observed tremor at Hakone in the next section.

Application to the seismic data at Hakone

We assumed the location of source model at the northern part of Hakone volcano (Fig. 5a) at a depth of 30 km

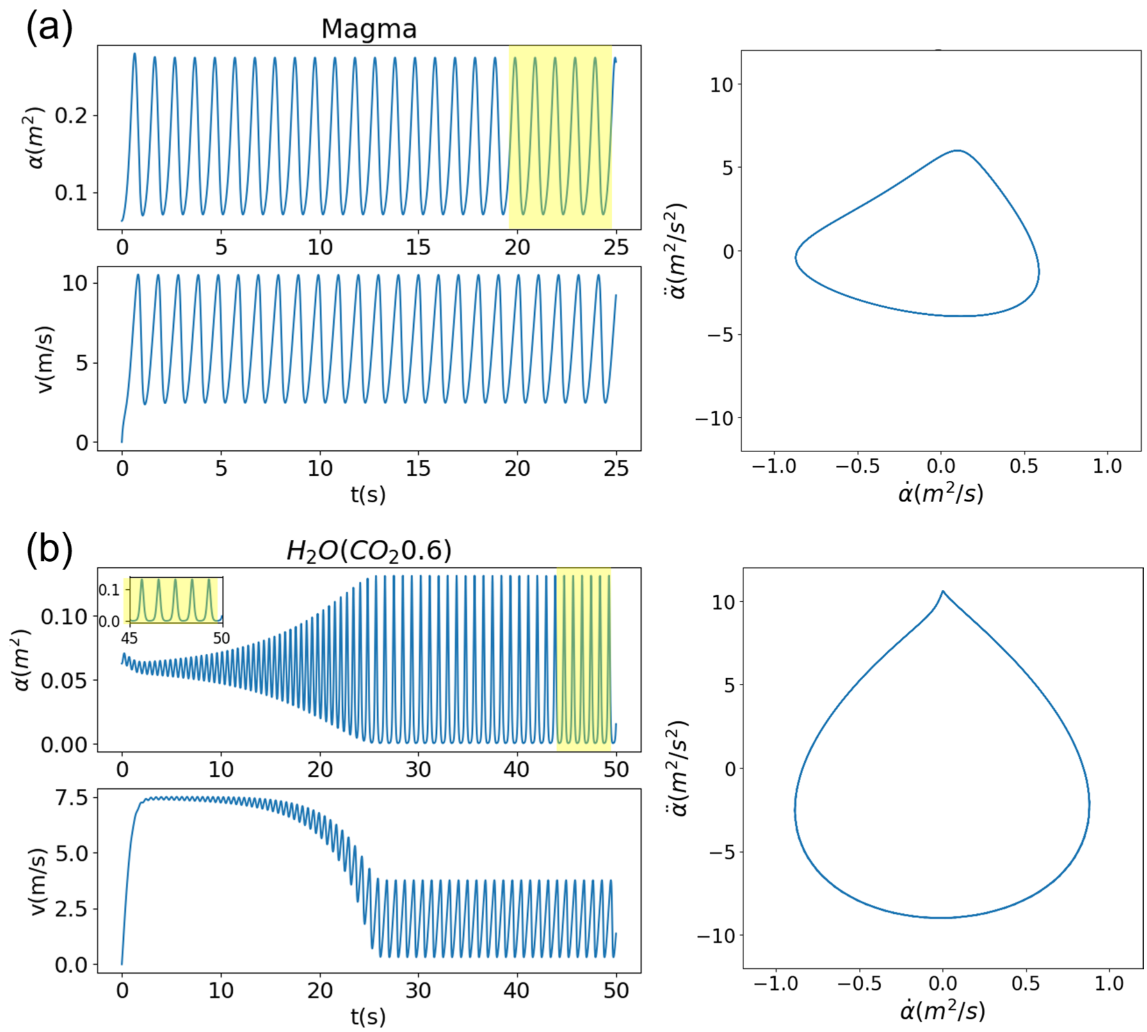

Fig. 4 Development of the channel oscillation by flow of magma (**a**) and super-critical fluid (**b**). The cross-sectional area, α, and the flow velocity, v, are shown as functions of the lapse time. The inset in (**b**) shows a magnified waveform of α from 45 to 50 s. The parameter values are listed in Tables 1 and 2, and $\alpha_s = 0.153$ and 0.059 m^2 for (**a**) and (**b**), respectively. Phase portraits $(\dot{\alpha}, \ddot{\alpha})$ are shown using the waveforms in the yellow-colored period (**a**: 20–25 s, **b**:45–50 s)

(Yukutake et al. 2022). The Green's functions at some stations are calculated and the one at the OMZ station is presented in Fig. 5b as an example. We took the convolution of the calculated $\Delta\alpha = \alpha - \alpha_0$ (Fig. 4) multiplied by $3k_r L$ (see Eq. 8) and the Green's function normalized by the assumed moment value, $M_0 = 10^9$ Nm, to obtain the model waveforms to be compared with the observation. We used $k_r = 7.61$ GPa, ten times smaller than the host rock value, to make the calculated amplitude similar to the observation, which is discussed later.

Figure 6 compares the calculated waveforms and the observations at three selected stations. Although the source waveform has only a single peak in each cycle (Fig. 4), the convoluted waveform has an apparent secondary peak. The previous models can generate similar waveforms exhibiting alternative large and small peaks by a non-linear effect of period-doubling (Julian 1994; Takeo 2020). However, the waveform in Fig. 6 is not due to the period-doubling but due to the amplification of the second mode due to the medium structure.

The calculated ground displacement became much larger than the observation if we used the bulk modulus of the rock ($k_r = 76.1$ GPa). Even if we used the Green's function with a possible lower Q, the calculated amplitudes were reduced only by factors (Fig. 7). When R is only slightly above unity, namely the condition is close to the oscillation limit, the amplitude is smaller. However, the waveform of α becomes sinusoidal so that the

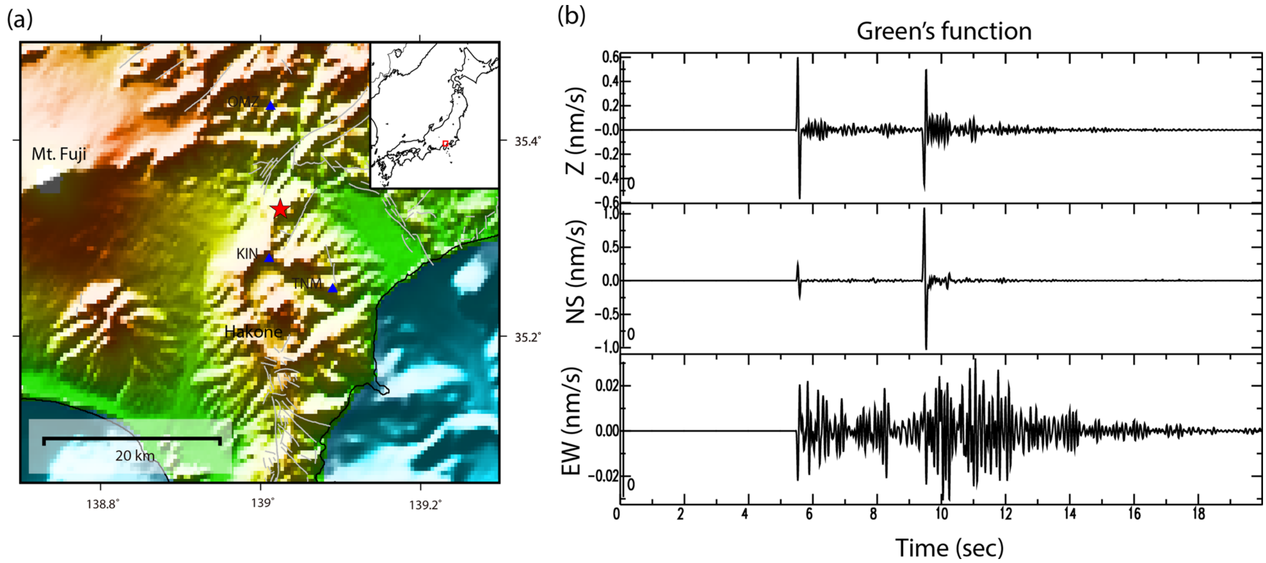

Fig. 5 **a** Map of Hakone volcano. Triangles show the locations of seismic stations. Red star shows the optimal epicenter of volcanic tremor estimated by Yukutake et al. (2022). To calculate the Green's function, we assumed a vertical open crack with EW strike (*y*-direction) at a depth of 30 km beneath the optimal epicenter. The inset indicates the target region for the Japanese Island. **b** The synthetic Green's function at OMZ station

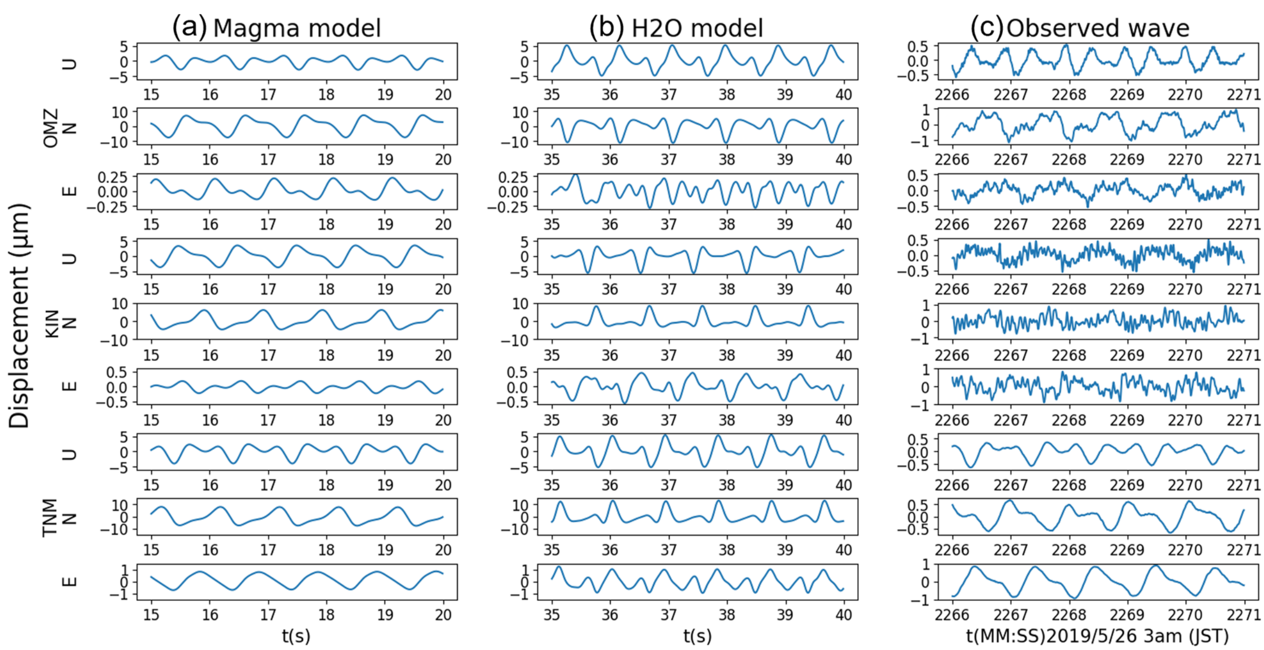

Fig. 6 Comparison of the calculated ground displacement waveforms and the observations at OMZ, KIN, and TNM stations (Fig. 5a). The left and central columns display the convolutions between the Green's function at each station and $\alpha(t)$ in Fig. 4a for magma and Fig. 4b for super-critical fluid, respectively. The right column shows the observed ground velocity

convolved waveforms at the stations do not have overtones and are less similar to the observed waveforms than the example in Fig. 6. We discuss the assumption of the smaller k_r in the next section.

Discussion

The small channel elasticity

The modified J94 model of this study was able to generate tremor around 1 Hz for either of magma or hydrothermal fluid with the range of parameter values presented

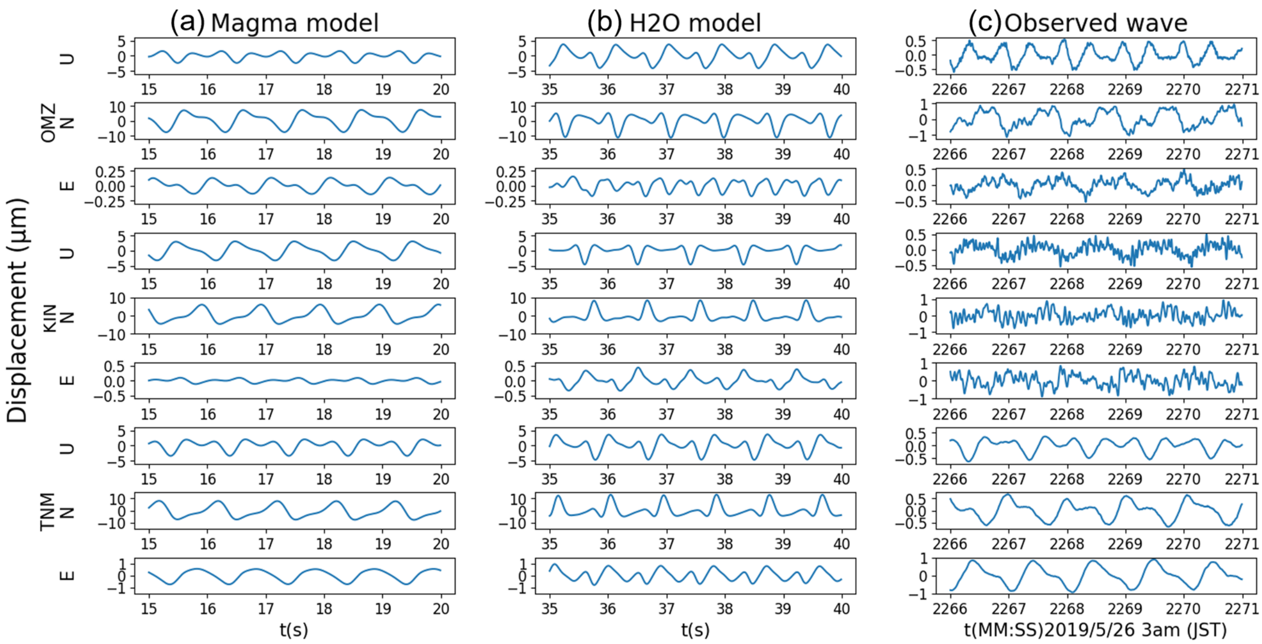

Fig. 7 Comparison of the calculated waveforms assuming the one-dimensional attenuation model based on the result by Kashiwagi et al. (2020) and the observations at OMZ, KIN, and TNM stations. The meaning of each column is same as that in Fig. 6

in Figs. 2 and 3 and Tables 1 and 2. The material parameters of the rock and the fluids are realistic except the crack elasticity, $K_c k_r$ (Fig. 2b), Even though K_c can be much smaller than unity for a thin crack, the values of K_c in the order of 10^{-6}–10^{-7} are too small. For example, a thin ellipsoidal crack of $4 \times 1 \times 0.02$ m^3 has $K_c \sim 0.017$ (Mizuno et al. 2016).

In the original model of J94, the corresponding parameter of K_c, which was the ratio of k' in Eq. (1) to k_r, was assumed in the order of 0.01. Figure 9 of J94 shows oscillation at ~ 5 Hz, which is realized with a longer channel ($L = 10$ m) with a larger inertia, $M' = 3 \times 10^5$ kg m^{-1}, where M' in Eq. (1) was approximated by $\rho_r L^2$ (Julian 1994). Equation (12) defines the corresponding inertia parameter of the elastic wall in Eq. (2) as $M_j = C_m \rho_r \alpha_0$, where $C_m \sim 1$ (Appendix 1 and Tables 1 and 2). The inertia coefficient scaled by ρ_r and the channel cross-sectional area is consistent with Corona-Romero et al. (2012), who formulated the flow-induced tremor model in a circular pipe. Then, $M_j \ll \rho_r L^2$, which is, for magma, much smaller than the inertia coefficient of fluid in the channel, $m_j \sim \rho L^2/12$, defined in Eq. (12). Considering this condition and the observed amplitude of the tremor signals at Hakone, Appendix 2 mathematically shows that the current model cannot generate oscillation at $f \sim 1$ Hz with K_c larger than 10^{-6}.

The small K_c indicates that the channel is more deformable than the expectation from the shape and the host rock property. When the host rock contains fluid in deformable configurations like partial melt network (Takei 2002) or fracture meshes (Sibson 1996), the effective elasticity can be reduced significantly (Mavko et al. 1998; Takei 2002). Although these mechanisms may explain the ten-times smaller k_r we used to calculate the ground displacement amplitudes similar to the observations (Figs. 6, 7), they may not generate the rock elasticity as small as $\sim 10^5$ Pa.

The sharp edges of the channel might be damaged or melted by the stress concentration, so the channel might have lost the elasticity of the rock. If the driving fluid is magma, it cannot penetrate the sharp edges due to its viscosity. Then, cavities filled with low-pressure volatiles exsolving from magma are generated at the tip and control the crack dynamics (Rubin 1993; Rubin and Gillard 1998). We assume cavities at both ends of the thin channel at $(y, z) = (0, \pm b_0)$ (Fig. 1). The cross-sectional area of each cavity on the yz-plane is α_c, and the cavity length along the z-axis is b_c. The cavity is filled with super-critical fluids at pressure, P_c, of which bulk modulus is approximated by P_c. When the channel expands, α_c also increases by $\Delta\alpha_c$. Then, the cavity pressure decreases by ΔP_c such that

$$\Delta P_c = -P_c \frac{\Delta \alpha_c}{\alpha_c}. \tag{22}$$

This pressure change acts as a spring to pull the channel wall inward. Assuming that $P_c \sim 500$ MPa and representing $\Delta\alpha_c/\alpha_c = \epsilon(\alpha - \alpha_0)/\alpha_0$ and $b_c = \beta b_0$, where ϵ and β are small constants, we may obtain the effective channel elasticity ($K_c k_r$) as $\epsilon\beta P_c$. The small elasticity is realized if $\epsilon\beta$ is small enough.

The above is one possible way to explain the small K_c for magma. It may not work when the oscillation is driven by super-critical fluids. What we want to emphasize here is that the channel elasticity may not be determined by the material property of rock alone but by the structure consisting of the rock and fluids. To fully validate the current flow-induced oscillation model as the mechanism of the deep harmonic tremor at Hakone, we need to specify a mechanical and material model that explain the small K_c, which is our future work.

Implications for tremor observation at Hakone

We extended J94 model to deal with turbulent flow. The magma flow was laminar, while the hydrothermal fluid flow was turbulent. We found that both of basaltic magma and hydrothermal fluids can generate similar flow-induced oscillation with similar channel dimensions (Tables 1, 2 and Fig. 7), regardless of their contrasting viscosity. This means that we cannot identify the nature of the source fluid. Due to the different viscosity, the effective pressures required to drive the flow were different by an order. In the case of the hydrothermal flow, the effective pressure was in the same order as the buoyancy of the fluid in the mantle rock ($p_1 \sim (\rho_r - \rho)gL$). In the case of magma, extra overpressure is sustained due to the viscosity. The overpressure in the order of 0.1 MPa (Table 1) is small compared to the lithostatic pressure at the tremor source depths (~ 500 MPa), so that it will not be observed.

Yukutake et al. (2022) show that the tremor signal at Hakone has a broad peak around 1.2 Hz during the initial part, while it represents the harmonic feature and the frequency gliding from 0.90 to 0.98 Hz at fundamental mode in the latter part. Then, the tremor terminated abruptly. These features were also reported for shallow harmonic tremors (Hotovec et al. 2013; Konstantinou et al. 2019; Takeo 2020). The flow-induced oscillation model like J94 and the current one may explain the transition between the broadband tremor and harmonic tremor (Konstantinou et al. 2019). Takeo (2020) reproduced the change of tremor waveform and amplitude by the change of the effective pressure. The harmonic tremor evolution at Hakone might also be explained by the change of conditions. In case of the magma flow, the shortening of L generates upward frequency gliding, while the decrease of p_1 can bring the condition from oscillation ($R > 1$) to non-oscillation ($R < 1$), keeping f at 1 Hz (Fig. 2a). On the other hand, in the hydrothermal system, the decrease of either L or p_1 may generate the upward frequency gliding (Fig. 3). Although the transition to chaos with the period doubling was the most interesting feature of J94 model, the current model did not exhibit such transitions, at least with the parameter ranges we tested. Thorough investigations of the behavior of the current model is beyond the scope of this study.

Yukutake et al. (2022) also reported that the deep LFEs within the depth ranges of 20–30 km above the tremor source region activated several hours prior to the occurrence time of volcanic tremor, suggesting that the fluid was supplied before the volcanic tremor. According to the results of theoretical modeling, the observed sequence might reflect the following procedure of fluid flow at the deep root of the volcano. At the onset of the activation for the deep LFEs, the supply of magmatic fluid started. At this timing, p_1 is not large enough to cause oscillation in the channel and the fluid flow triggered only the deep LFEs. At the start time of the volcanic tremor, p_1 increased, leading to oscillation of the channel. Moreover, during the latter part of the tremor, shortening of L or decrease in p_1 caused the frequency gliding in the harmonic tremor. Finally, the abrupt termination of tremor amplitude occurred due to decrease in p_1.

Conclusions

We extended the flow-induced oscillation model of Julian (1994) to incorporate the realistic material parameters beneath a volcano and to link the model waveforms to the seismometer data. Applying the model to the deep harmonic tremor observed at Hakone volcano, we obtained the following conclusions.

(1) Both magma and super-critical fluids can generate tremors with realistic material and flow parameters and channel sizes (widths of centimeters and lengths of meters).
(2) The model waveforms convolved with the Green's function at each seismic station reproduced the observed waveform features.
(3) Although the source waveform had only a single peak at each cycle, the convolved waveform exhibited an apparent secondary peak, which was similar to the observed waveforms. While the previous models generated similar waveforms exhibiting alternative large and small peaks by a non-linear effect of period-doubling before the chaos, our

model did not show such transitions, at least with the investigated parameters.

(4) Although most of the parameters and physical values of the solutions were in the realistic ranges, the effective elasticity of the channel as small as 10^5 Pa was required to generate oscillation at ~ 1 Hz. Also, we needed to assume a smaller bulk modulus around the channel to obtain the ground displacement amplitudes at the stations similar to the observation. The small channel elasticity and bulk modulus might be generated by the presence of compressible fluids in the system. To fully validate our model, the mechanism of such small elasticity should be identified, which is our future work.

Appendix 1: Effective mass of the channel wall

We derive the effective mass coefficient, C_m, used in the equation of motion of the channel wall (Eq. 2), by the analogy of the equation of motion for bubble expansion in fluid (Plesset and Prosperetti 1977; Prosperetti 1982). First, we consider the spherical expansion of a source with a radius, S, and a volume, $V = 4\pi S^3/3$. Approximating that the deformation around the source is incompressible,

$$r^2 v_r = S^2 \dot{S} = \frac{\dot{V}}{4\pi}, \tag{23}$$

where v_r is the radial velocity at a distance r from the center of the sphere. The equation of motion for the spherical bubble expansion is derived by integrating the radial component of Navier-Stokes equation. For simplicity, we neglect the non-linear advection term, so that

$$\rho_r \int_S^\infty \frac{\partial v_r}{\partial t} \mathrm{d}r = p_i - p_\infty + 3 \int_S^\infty \frac{\tau_{rr}}{r} \mathrm{d}r, \tag{24}$$

where p_i and p_∞ are the pressure in the bubble and in the medium at $r = \infty$, respectively, and τ_{rr} is the deviatoric stress. Substituting v_r in Eq. (23), the inertia term of (24) is

$$\rho_r \int_S^\infty \frac{\partial v_r}{\partial t} \mathrm{d}r = \frac{\rho_r \ddot{V}}{4\pi S}. \tag{25}$$

We use Eq. (25) as the inertia term of the channel expansion, $C_m \rho_r \ddot{\alpha}$, by replacing $\ddot{V}$ by the volume acceleration of the channel, $\ddot{V} = L\ddot{\alpha}$, with an approximation of $(4\pi/3)S^3 \sim \alpha_0 L$. Namely, we use the following equations to obtain Eq. (4):

$$C_m \rho_r \ddot{\alpha} = \frac{\rho_r L \ddot{\alpha}}{4\pi S}, S^3 \sim \frac{3\alpha_0 L}{4\pi}. \tag{26}$$

Appendix 2: Possible range of K_c that generates tremor around 1 Hz

We calculated the channel oscillations with $L \sim 4$ m (Tables 1 and 2) and obtained the amplitudes of $\Delta\alpha \sim 10^{-1}$ m^2. The corresponding seismic moment is $k_r L \Delta\alpha \sim 10^{10}$ Nm. The calculated ground displacement at the stations were too large, so that we used $k_r = 7.61$ GPa instead of 76.1 GPa in Figs. 6 and 7. Yet, the calculated waveforms are about ten times larger than the observed seismic amplitude (Yukutake et al. 2022). This means that the expected value of $L\Delta\alpha$ is $\sim 10^{-2}$. Assuming that $\Delta\alpha$, α_0, and α_s are all in the same order,

$$L\Delta\alpha \sim L\alpha_s \sim L\alpha_0 = L\pi a_0 b_0 \sim 10^{-2}. \tag{27}$$

We consider a thin channel with $a_0/b_0 < 10^{-2}$ with the length L in the same order as b_0. Then, we may estimate from (27) as $L \sim b_0 \geq 1$.

We use these estimations to rearrange the equations obtained by the stability analysis; Eqs. (11)–(19). Below we assume $A = 0$ for simplicity. Using (12) with (4) and above approximation, we obtain

$$\begin{aligned} M_j &= \rho_r \left(\frac{L^2 \alpha_0^2}{48\pi^2} \right)^{\frac{1}{3}} \sim \rho_r \left(\frac{10^{-4}}{48\pi^2} \right)^{\frac{1}{3}} \\ &\sim \frac{\rho_r}{4.73^{1/3}} \times 10^{-2} \sim 20, \end{aligned} \tag{28}$$

$$m_j \sim \frac{\rho L^2}{12}, \tag{29}$$

$$\frac{M_j}{m_j} \sim \frac{240}{\rho L^2} \ll 1. \tag{30}$$

Below we approximate $M_j + m_j \sim m_j$.

Equation (20) gives $C_1 \sim (2\pi f_i)^2$, where f_i is the frequency at the onset of instability. It is noted that, in the non-linear regime, the frequency f determined from the numerical solution is smaller than f_i by a factor. For example, with the parameter set in Table 1 that generates the solution in Fig. 4a gives $C_1 \sim 320$, which yields $f_i \sim 2.8$ Hz. Equation (17) is transformed to

$$K_c k_r \sim [(2\pi f_i)^2 - (\Gamma + 2e)\Gamma] m_j \sim [(2\pi f_i)^2 - (\Gamma + 2e)\Gamma] \frac{\rho L^2}{12}, \tag{31}$$

Also, we rewrite the tremor condition (19) as

$$K_c k_r < \rho v_s^2 \left(2 + \frac{e}{\Gamma}\right) - 2(\Gamma + 2e)(\Gamma + e)\frac{\rho L^2}{12}, \quad (32)$$

From the definition (13) and (14),

$$\Gamma \sim \frac{4\eta}{a_0^2 \rho}, e \sim \frac{C_d v_s}{4a_0}. \quad (33)$$

For magma, Γ dominates e. Then, Eqs. (31) and (32) become

$$K_c k_r \sim [(2\pi f_i)^2 - \Gamma^2]\frac{\rho L^2}{12} < 2\rho v_s^2 - 2\Gamma^2 \frac{\rho L^2}{12} \quad (34)$$

We consider the realistic magma flow speed v_s to be smaller than a few meters per second, namely, $v_s^2 < 10$. Then, with $\rho = 2800$ kg/m^3, Eq. (34) requires $K_c k_r < 2\rho v_s^2 < 5.6 \times 10^4$ Pa, which yields $K_c < 10^{-6}$. Equation (34) with (33) also requires

$$\frac{4\eta}{a_0^2 \rho} < 2\pi f_i, \quad (35)$$

$$L^2 < \frac{24 v_s^2}{(2\pi f_i)^2 + \Gamma^2} < \frac{24 v_s^2}{(2\pi f_i)^2}. \quad (36)$$

The relationships (35), (36), and (27) along with the magma properties (Table 1) require that a_0 should be larger than the order of 0.01, and b_0 and L should be smaller than several meters. It means that we cannot assume an extremely thin channel to allow K_c to be small.

On the other hand, $\Gamma \ll e$ for hydrothermal fluid. Then, Eq. (31) becomes and (32) become

$$K_c k_r \sim [(2\pi f_i)^2 - 2e\Gamma]\frac{\rho L^2}{12} < \rho v_s^2 \frac{e}{\Gamma} - 4e^2 \frac{\rho L^2}{12} \quad (37)$$

The inequality relation of (37) is transformed with (33) to

$$\frac{\rho L^2}{12} < \frac{\rho v_s^2}{(4\pi f_i)^2 + 4e^2}\frac{e}{\Gamma} < \frac{\rho v_s^2}{4e\Gamma} \sim \frac{\rho^2 a_0^3 v_s}{4\eta C_d}. \quad (38)$$

Using the relationship (38) and (37), one obtains

$$K_c k_r < (2\pi f_i)^2 \frac{\rho^2 a_0^3 v_s}{4\eta C_d} \sim 10^4 v_s, \quad (39)$$

using the parameter values in Table 2 and assuming $a_0 < 0.01$ m. The conditions that generate tremors comparable with the observations yield $v_s < 10$ m/s. though v_s of the hydrothermal fluid can be larger. Then, we estimate $K_c \leq 10^{-6}$.

Supplementary Information

The online version contains supplementary material available at https://doi.org/10.1186/s40623-023-01865-w.

Additional file 1. Delivation of the basic equations.

Acknowledgements
The authors thank Minoru Takeo for valuable discussions and checking the numerical solutions. The manuscript has been significantly improved by the valuable comments from the associate editor, K. I. Konstantinou, and two anonymous reviewers. The observed waveforms presented in Figs. 6 and 7 were recorded at the seismic station installed by the Hot Springs Research Institute of Kanagawa Prefecture.

Author contributions
TO derived the model equations, performed the model calculations, and created all figures except Fig. 5. YY provided the observation detail at Hakone volcano, calculated the Green's functions, and created Fig. 5. MI initiated this study and gave the theoretical basis of the study. All authors wrote and discussed the manuscript.

Funding
The present study was supported by JSPS KAKENHI Grant No. 22K18728 (MI) and 22K0375 (YY).

Data availibility
Not applicable because this is a theoretical study.

Declarations

Competing interests
The authors declare no competing interests.

Author details
[1]Earthquake Research Institute, University of Tokyo, Tokyo 113-0032, Japan.

Received: 27 December 2022 Accepted: 28 June 2023
Published online: 17 July 2023

References

Aki K, Koyanagi R (1981) Deep volcanic tremor and magma ascent mechanism under Kilauea, Hawaii. J Geophys Res 86:7095–7109. https://doi.org/10.1029/JB086iB08p07095

Aki K, Richards PG (2002) Quantitative seismology, 2nd edn. University Science Books, Ausalito, CA

Aso N, Ohta K, Ide S (2013) Tectonic, volcanic, and semi-volcanic deep low-frequency earthquakes in western Japan. Tectonophysics 600:27–40. https://doi.org/10.1016/j.tecto.2012.12.015

Audétat A, Keppler H (2004) Viscosity of fluids in subduction zones. Science 303:513–516. https://doi.org/10.1126/science.1092282

Bowers TS (1995) Pressure-volume-temperature properties of H_2O-CO_2 fluids. In: Ahrens TJ (ed) A handbook of physical constants: rock physics and phase relations. AGU reference shelf series, vol 3. AGU, pp 45–72

Chouet BA (1996) New methods and future trends in seismological volcano monitoring. In: Scarpa R, Tilling RI (eds) Monitoring and mitigation of volcano hazards. Springer, Berlin, pp 23–97. https://doi.org/10.1007/978-3-642-80087-0_2

Chouet B (1988) Resonance of a fluid-driven crack: radiation properties and implications for the source of long-period events and harmonic tremor. J Geophys Res 93:4375–4400. https://doi.org/10.1029/JB093iB05p04375

Christensen NI (1996) Poisson's ratio and crustal seismology. J Geophys Res 101:3139–3156. https://doi.org/10.1029/95JB03446

Corona-Romero P, Arciniega-Ceballos A, Sánchez-Sesma FJ (2012) Simulation of LP seismic signals modeling the fluid–rock dynamic interaction. J

Volcanol Geotherm Res 211–212:92–111. https://doi.org/10.1016/j.jvolgeores.2011.09.002
Dunham EM, Ogden DE (2012) Guided waves along fluid-filled cracks in elastic solids and instability at high flow rates. J Appl Mech 79:031020. https://doi.org/10.1115/1.4005961
Ferrazzini V, Aki K (1987) Slow waves trapped in a fluid-filled infinite crack: implications for volcanic tremor. J Geophys Res 92:9215–9223
Fujita E (2008) Banded tremor at Miyakejima volcano, Japan: implication for two-phase flow instability. J Geophys Res 113:B04207. https://doi.org/10.1029/2006JB004829
Girona T, Caudron C, Huber C (2019) Origin of shallow volcanic tremor: the dynamics of gas pockets trapped beneath thin permeable media. J Geophys Res 124:4831–4861. https://doi.org/10.1029/2019JB017482
Hagerty M, Benites R (2003) Tornillos beneath Tongariro Volcano, New Zealand. J Volcanol Geotherm Res 125:151–169. https://doi.org/10.1016/S0377-0273(03)00094-5
Hasegawa A, Yamamoto A (1994) Deep, low-frequency microearthquakes in or around seismic low-velocity zones beneath active volcanoes in northeastern Japan. Tectonophysics 233:233–252. https://doi.org/10.1016/0040-1951(94)90243-7
Hellweg M (2000) Physical models for the source of Lascar's harmonic tremor. J Volcanol Geotherm Res 101:183–198. https://doi.org/10.1016/S0377-0273(00)00163-3
Hiraga S (1987) Seismicity of Hakone volcano and its adjacent area. Bull Hot Springs Res Inst Kanagawa Pref 18:149–273 (**in Japanese**)
Hotovec AJ, Prejean SG, Vidale JE, Gomberg J (2013) Strongly gliding harmonic tremor during the 2009 eruption of Redoubt Volcano. J Volcanol Geotherm Res 259:89–99. https://doi.org/10.1016/j.jvolgeores.2012.01.001
Ichihara M, Lyons JJ, Yokoo A (2013) Switching from seismic to seismo-acoustic harmonic tremor at a transition of eruptive activity during the Shinmoedake 2011 eruption. Earth Planets Space 65:633–643. https://doi.org/10.5047/eps.2013.05.003
Ichihara M, Kusakabe T, Kame N, Kumagai H (2016) On volume-source representations based on the representation theorem. Earth Planets Space 68:14. https://doi.org/10.1186/s40623-016-0387-3
Ichimura M, Yokoo A, Kagiyama T, Yoshikawa S, Inoue H (2018) Temporal variation in source location of continuous tremors before ash-gas emissions in January 2014 at Aso volcano, Japan. Earth Planets Space 70:125. https://doi.org/10.1186/s40623-018-0895-4
Iwanuma K, Kaneshima S (2005) Numerical simulation of the steam-water flow instability as a mechanism of long-period ground vibrations at geothermal areas. Geophys J Int 163:833–851. https://doi.org/10.1111/j.1365-246X.2005.02749.x
Jellinek AM, Bercovici D (2011) Seismic tremors and magma wagging during explosive volcanism. Nature 470:522–525. https://doi.org/10.1038/nature09828
JSME (1983) Data book: thermophysical properties of fluids. The Japan Society of Mechanical Engineers
Julian BR (1994) Period doubling and other nonlinear phenomena in volcanic earthquakes and tremor. J Volcanol Geotherm Res 101:19–26. https://doi.org/10.1029/93JB03129
Julian BR (2000) Volcanic tremor: nonlinear excitation by fluid flow. J Geophys Res 99:11859–11877. https://doi.org/10.1016/S0377-0273(00)00165-7
Kamo K, Furuzawa T, Akamatsu J (1977) Some natures of volcanic microtremors at the Sakura-jima volcano. Bull Volcanol Soc Jpn 22:41–58 (**in Japanese with English abstract**)
Kashiwagi H, Nakajima J, Yukutake Y, Honda R, Abe Y, Sakai S (2020) Seismic constraint on the fluid-bearing systems feeding Hakone Volcano, Central Japan. J Geophys Res Solid Earth 125:e2020JB020341. https://doi.org/10.1029/2020JB020341
Kodaira S, Sato T, Takahashi N, Ito A, Tamura Y, Tatsumi Y, Kaneda Y (2007) Seismological evidence for variable growth of crust along the Izu intraoceanic arc. J Geophys Res. https://doi.org/10.1029/2006jb004593
Konstantinou KI (2002) Deterministic non-linear source processes of volcanic tremor signals accompanying the 1996 Vatnajökull eruption, central Iceland. Geophys J Int 148:663–675. https://doi.org/10.1046/j.1365-246X.2002.01608.x
Konstantinou KI (2015) Tornillos modeled as self-oscillations of fluid filling a cavity: application to the 1992–1993 activity at Galeras volcano, Colombia. J Volcanol Geotherm Res 238:23–33. https://doi.org/10.1016/j.pepi.2014.10.014
Konstantinou KI, Schlindwein V (2002) Nature, wavefield properties and source mechanism of volcanic tremor: a review. Phys Earth Planet Int 119:161–187. https://doi.org/10.1016/S0377-0273(02)00311-6
Konstantinou KI, Astrid Ardiani M, Sudibyo MRP (2019) Scaling behavior and source mechanism of tremor recorded at Erebus volcano, Ross island, Antarctica. Phys Earth Planet Int 290:99–106. https://doi.org/10.1016/j.pepi.2019.03.010
Landau LD, Lifshitz EM (1987) Fluid mechanics, 2nd edn. Pergamon Press, Oxford
Lees JM, Gordeev EI, Ripepe M (2004) Explosions and periodic tremor at Karymsky volcano, Kamchatka, Russia. Geophys J Int 158:1151–1167. https://doi.org/10.1111/j.1365-246X.2004.02239.x
Leet RC (1988) Saturated and subcooled hydrothermal boiling in groundwater flow channels as a source of harmonic tremor. J Geophys Res 93:4835–4849. https://doi.org/10.1029/JB093iB05p04835
Lipovsky BP, Dunham EM (2015) Vibrational modes of hydraulic fractures: inference of fracture geometry from resonant frequencies and attenuation. J Geophys Res 120:1080–1107. https://doi.org/10.1002/2014JB011286
Lyons JJ, Ichihara M, Kurokawa A, Lees JM (2013) Switching between seismic and seismo-acoustic harmonic tremor simulated in the laboratory: insights into the role of open degassing channels and magma viscosity. J Geophys Res 118:277–289. https://doi.org/10.1002/jgrb.50067
Maeda T, Takemura S, Furumura T (2017) OpenSWPC: an open-source integrated parallel simulation code for modeling seismic wave propagation in 3D heterogeneous viscoelastic media. Earth Planets Space 69:102. https://doi.org/10.1186/s40623-017-0687-2
Maryanto S, Iguchi M, Tameguri T (2008) Constraints on the source mechanism of harmonic tremors based on seismological, ground deformation, and visual observations at Sakurajima volcano, Japan. J Volcanol Geotherm Res 170:198–217. https://doi.org/10.1016/j.jvolgeores.2007.10.004
Matoza RS (2020) Seismicity from the deep magma system. Science 368:708–709. https://doi.org/10.1126/science.abc2452
Matsumoto S, Shimizu H, Matsushima T, Uehira K et al (2013) Short-term spatial change in a volcanic tremor source during the 2011 Kirishima eruption. Earth Planets Space 65:323–329. https://doi.org/10.5047/eps.2012.09.002
Mavko G, Mukerji T, Dvorkin J (1998) The rock physics handbook, Tools for seismic analysis in porous media. Cambridge University Press, Cambridge
Mizuno N, Ichihara M, Kame N (2015) Moment tensors associated with the expansion and movement of fluid in ellipsoidal cavities. J Geophys Res 120:6058–6070. https://doi.org/10.1002/2015JB012084
Mizuno N, Kame N, Ichihara M (2016) Ellipsoidal volume source calculation webtool for moment tensor evaluation of three models: (1) expansion, (2) simple movement of magma and (3) pressure recovery after simple movement. Bull Volcanol Soc Jpn 61:449–457. https://doi.org/10.18940/kazan.61.2_449. (**in Japanese with English abstract**)
Natsume Y, Ichihara M, Takeo M (2018) A non-linear time-series analysis of the harmonic tremor observed at Shinmoedake volcano, Japan. Geophys J Int 216:1768–1784. https://doi.org/10.1093/gji/ggy522
Nichols ML, Malone SD, Moran SC, Thelen WA, Vidale JE (2011) Deep long-period earthquakes beneath Washington and Oregon volcanoes. J Volcanol Geotherm Res 200:116–128. https://doi.org/10.1016/j.jvolgeores.2010.12.005
Oikawa G, Aso N, Nakajima J (2021) Depth dependent focal mechanisms of volcanic deep low-frequency earthquakes in Northeast Japan. J Geophys Res 126:12. https://doi.org/10.1029/2021JB022666
Plesset MS, Prosperetti A (1977) Bubble dynamics and cavitation. Ann Rev Fluid Mech 9:145–185. https://doi.org/10.1146/annurev.fl.09.010177.001045
Prosperetti A (1982) A generalization of the Rayleigh–Plesset equation of bubble dynamics. Phys Fluids 25:409–410. https://doi.org/10.1063/1.863775
Ripepe M, Delle Donne D, Lacanna G, Marchetti E, Ulivieri G (2009) The onset of the 2007 Stromboli effusive eruption recorded by an integrated geophysical network. J Volcanol Geotherm Res 182:131–136. https://doi.org/10.1016/j.jvolgeores.2009.02.011
Rubin AM (1993) Dikes vs. diapirs in viscoelastic rock. Earth Planet Sci Lett 117:653–670. https://doi.org/10.1016/0012-821X(93)90109-M
Rubin AM, Gillard D (1998) Dike-induced earthquakes: theoretical considerations. J Geopys Res 103:10017–10030. https://doi.org/10.1029/97JB03514

Rust AC, Balmforth NJ, Mandre S (2008) The feasibility of generating low-frequency volcano seismicity by flow through a deformable channel. Geol Soc Lond Spec Publ 307:45–56. https://doi.org/10.1144/sp307.4
Sibson RH (1996) Structural permeability of fluid-driven fault-fracture meshes. J Struct Geol 18:1031–1042. https://doi.org/10.1016/0191-8141(96)00032-6
Takei Y (2002) Effect of pore geometry on V_P/V_S: from equilibrium geometry to crack. J Geophys Res 107(B2):2043. https://doi.org/10.1029/2001jb000522
Takeo M (2020) Harmonic tremor model during the 2011 Shinmoe-dake eruption, Japan. Geophys J Int 224:2100–2120. https://doi.org/10.1093/gji/ggaa477
Ukawa M, Ohtake M (1987) A monochromatic earthquake suggesting deep-seated magmatic activity beneath the Izu-Ooshima Volcano, Japan. J Geophys Res 92:12649–12663. https://doi.org/10.1029/JB092iB12p12649
Wilson L, Sparks RSJ, Walker GPL (1980) Explosive volcanic eruptions—IV. The control of magma properties and conduit geometry on eruption column behaviour. Geophys J Int 63:117–148. https://doi.org/10.1111/j.1365-246X.1980.tb02613.x
Yamada T, Kurokawa AK, Terada A, Kanda W, Ueda H, Aoyama H, Ohkura T, Ogawa Y, Tanada T (2021) Locating hydrothermal fluid injection of the 2018 phreatic eruption at Kusatsu-Shirane volcano with volcanic tremor amplitude. Earth Planets Space 73:14. https://doi.org/10.1186/s40623-020-01349-1
Yoshida K, Hasegawa A, Noguchi S, Kasahara K (2020) Low-frequency earthquakes observed in close vicinity of repeating earthquakes in the brittle upper crust of Hakodate, Hokkaido, northern Japan. Geophys J Int 223:1724–1740. https://doi.org/10.1093/gji/ggaa418
Yukutake Y, Abe Y, Honda R, Sakai S (2021) Magma reservoir and magmatic feeding system beneath Hakone Volcano, Central Japan, revealed by highly resolved velocity structure. J Geophys Res 126:e2020JB021236. https://doi.org/10.1029/2020JB021236
Yukutake Y, Honda R, Ukawa M, Kurita K (2022) Harmonic tremor from the deep part of Hakone volcano. Earth Planets Space 74:144. https://doi.org/10.1186/s40623-022-01700-8

Publisher's Note

Springer Nature remains neutral with regard to jurisdictional claims in published maps and institutional affiliations.